A novel cast $Co_{68}Al_{18.2}Fe_{6.5}V_{4.75}Cr_{2.55}$ dual-phase medium entropy alloy with superior high-temperature performance

Xiangkui Liu [a,1], Shuai Feng [b,1], Huiqing Xu [a], Conghao Liu [a], Xulong An [a], Zhuqi Chu [a], Wei Wei [a], Dandan Wang [a], Yemao Lu [d], Zhenfei Jiang [c,*], Jian Kong [b,**]

[a] School of Materials Science and Engineering, Changzhou University, 1 Gehu Road, Changzhou, 213164, PR China
[b] School of Materials Science and Engineering, Nanjing University of Science and Technology, 200 Xiaolingwei, Nanjing, 210094, PR China
[c] National Engineering Research Center of Light Alloy Net Forming, Shanghai Jiao Tong University, 800 Dongchuan Road, Shanghai, 200240, PR China
[d] Institute of Nanotechnology, Karlsruhe Institute of Technology, D-76021, Karlsruhe, Germany

Keywords:
Medium-entropy alloy
Deformation mechanism
High-temperature properties
Microstructure

A B S T R A C T

A newly-designed $Co_{68}Al_{18.2}Fe_{6.5}V_{4.75}Cr_{2.55}$ medium entropy alloy (MEA) with FCC + B2 structure exhibits not only an excellent strength-ductility combination at room temperature, but also an outstanding high-temperature mechanical properties in particular. The phase formation, microstructure and deformation mechanism of this designed dual-phase MEA at room and high temperatures were investigated and discussed in detail. Based on experimental results (XRD, SEM and TEM) and theoretical analysis (calculated diagram and empirical thermodynamic parameters), it is demonstrated that this newly-designed MEA consists of a dual-phase structure of a face-centered-cubic (FCC) phase (70.3 vol %) plus chemically ordered body-centered cubic phase (B2) (29.7 vol %). Meanwhile, the FCC phase is enriched with Co, Fe and Cr elements, while the B2 phase is enriched with Al and Co elements. Furthermore, compared with some HEAs/MEAs and commercial alloys, this newly-designed dual-phase MEA exhibits excellent strength-ductility combination with a high compressive yield strength of ~1254 MPa, a fracture strength of ~2657 MPa and a large compressive plasticity of ~34.6 % at room temperature. In particular, the studied MEA also shows an outstanding high-temperature performance with an ultrahigh yield strength of ~1213 MPa at 600 °C and ~626 MPa at 800 °C, respectively. The excellent comprehensive mechanical properties of this designed dual-phase MEA at both room and temperatures mainly originate from synergy effect of alternate FCC + B2 structure and strengthening contributions of B2 phase. These important findings not only reveal the deformation and strengthening mechanisms of the newly-designed dual-phase MEA, but also provides an effective alloy design strategy for developing advanced structural materials serving as a wide range of temperature.

1. Introduction

The pursuit for high-strength and ductile structural materials has always been an everlasting aim in the field of metallurgy for a long time [1]. The traditional concept of alloy design is usually based on one or two principal elements, which may seriously limit the engineering application of alloys [2,3]. In order to achieve excellent balance of strength and ductility of metal materials, the traditional concept of alloy design is broken and high/medium-entropy alloys (HEAs/MEAs) based on multi-principal elements in equal or near-equal atomic ratios were proposed almost simultaneously by Yeh et al. [4] and Cantor et al., in 2004 [5]. As a new class of emerging alloys with a novel alloy design concept, most HEAs consist of at least five (or four) principal elements together with an atomic concentration of 5%–35 %, which has received widespread attention due to their unique properties [6,7], such as high strength and hardness [8,9], excellent corrosion resistance [10], etc. Usually, simple single face-centered cubic (FCC) and body-centered cubic (BCC) solid solutions form in HEAs, instead of complex intermetallic compounds, which can mainly be ascribed to its high configurational entropy effect [4]. However, single-phase HEAs generally show

* Corresponding author.
** Corresponding author.
E-mail addresses: jzf9@sjtu.edu.cn (Z. Jiang), kongjian68@126.com (J. Kong).
[1] These authors have equally contributed to this work.

unsatisfactory mechanical performance. For example, CrCoFeNiMn HEA with single-phase FCC structure usually exhibit excellent ductility but low strength, while HfNbTaTiZr HEA with single-phase BCC structure show high strength but low ductility [11,12]. Such simple-phase microstructure seriously affects the mechanical properties and the engineering application of HEAs.

How to overcome the trade-off of the strength and ductility in single-phase HEAs is still a huge challenge. Fortunately, the dual-phase HEAs containing FCC and BCC phases were proposed, which proved to be effective in improving the mechanical properties of HEAs. During the deformation process of the dual-phase HEAs, there is a synergistic effect in the soft FCC and hard BCC phases, obtaining an excellent matching of high strength and large plasticity in HEAs. For example, Lu et al. designed an $AlCoCrFeNi_{2.1}$ eutectic high entropy alloy (EHEA) with dual-phase lamellar microstructures combined by soft FCC and hard BCC phases [13], which not only shows good liquidity and castability but also exhibit excellent mechanical properties, i.e., tensile strength of 944 MPa and plastic strain with 25.6 %. Moreover, Li et al. reported that a metastable dual-phase $Fe_{50}Mn_{30}Co_{10}Cr_{10}$ HEA was designed by varying the Mn content in alloys system to generate transformation-induced plasticity (TRIP) [14]. In addition, Shi et al. fabricated a dual-phase ultrafine-grained EHEA through severe cold rolling and annealing treatment, which exhibited ultimate tensile strength of 1.6 GPa and ductility of 14 % [15,16]. However, the design concept of dual-phase HEAs is still elusive owing to the complex composition, making it difficult to predict the dual-phase structure in HEAs.

To obtain the dual-phase mixture of FCC/BCC structure, Guo et al. proposed that the valence electron configuration (VEC) value of the alloy should be in the range 6.87–8 (FCC + BCC) [17]. This is attributed to the empirical criterion between the VEC effect and the phase stability in solid solution forming HEAs, i.e., BCC phases are stabilized at a lower VEC range (<6.87), both FCC and BCC phases exist in the intermediate VEC (6.87 < VEC <8.0), while FCC phases are stabilized at a higher VEC (>8.0) [17]. Based on the above empirical rules, dual-phase FCC/BCC-structured HEAs was successfully designed by adjusting Al content in FCC-structured HEAs, accompanied by the VEC values in the range of 6.87–8.0 [18,19]. Besides, the mixing enthalpy method, the semi-quantitative method based on Calculation of Phase Diagram (CALPHAD) and equal molar ratio mixing method, etc. also provide vital guidance for the design of dual-phase HEAs [20–23].

High-temperature performance is one of engineering applications with great promise to dual-phase HEAs [24–26]. Dual-phase HEAs commonly exhibit superior strength at high temperatures when two phases have a coherent relationship [27,28]. In addition, many commercial alloys with outstanding high-temperature performance are based on the strengthen mechanism of second phase to achieve high strength at elevated temperature [29,30]. For example, the FCC matrix is usually strengthened by fine precipitates of a $Ni_3(Al, Ti)$ phase with an $L1_2$ structure in Ni-based superalloys [31]. Similarly, such microstructure can appear in some HEAs [32,33]. Recent studies indicated that some HEAs possess improved high-temperature performance compared with the conventional Ni-based superalloys [34]. Meanwhile, some HEAs accompanied by a BCC matrix with embedded B2 precipitates exhibit excellent mechanical performance at room and elevated temperatures together with large ductility owing to the reinforcement of BCC (B2) phase [35,36]. Thus, some dual-phase HEAs containing BCC (B2) phase may possess a promising potential for high-temperature applications.

In this work, we choose Co–Al–Fe–V–Cr as the base alloy system due to a large dual-phase region consisting of FCC and B2 phases in this alloy system. First, the addition of 18.2 at.% Al element can induce the formation of hard BCC phase, leading to a better synergistic strengthening effect. Second, the atomic radius of Al element is larger than that of Co, Fe, V and Cr elements, and the addition of Al element can cause larger lattice distortion, which can also strengthen this alloy to a certain extent. Third, the addition of Co, Fe, V and Cr elements can make the FCC matrix possess good stability so that this alloy maintains a stable FCC solid solution structure. thus, to design dual-phase eutectic or near-eutectic Co–Al–Fe–V–Cr alloys, a large number of phase diagram calculations based on CALPHAD were performed by adjusting the number of element atoms in the Co–Al–Fe–V–Cr alloy system. In order to obtain an MEA with promising potential applications at room temperature and high temperatures, we designed a novel $Co_{68}Al_{18.2}Fe_{6.5}V_{4.75}Cr_{2.55}$ dual-phase MEA, which has alternant dual-phase structure of FCC + B2 phases. The as-designed dual-phase MEA not only exhibits high room-temperature strength and large ductility, but also shows excellent high-temperature properties. The mechanical properties of the as-designed dual-phase MEA at room temperature and high temperature of 600 °C and 800 °C were investigated in detail in this work.

2. Experimental procedure

The ingot of the $Co_{68}Al_{18.2}Fe_{6.5}V_{4.75}Cr_{2.55}$ alloys were fabricated by arc-melting the mixtures of high-purity constituent elements in a Ti-gettered argon atmosphere and the ingot was remelted at least five times to ensure chemical homogeneity. Following the last re-melting step, the melt was drop-cast in a rectangular copper mold of dimensions: 60 mm × 10 mm × 5 mm (height × length × width). The as-cast MEA was characterized by Bruker D8 X-ray diffractometry (XRD) with Cu Kα radiation and the scanning range of 2θ is 20°–100°. The samples were ground with SiC abrasive papers with grits of 400, 800, and 1,200, and finally polished with 0.25-μm-diamond suspension. The microstructure and fracture morphology of the as-cast MEA were observed by FEI Quanta 250F scanning electron microscope (SEM) with SE detector. Corresponding chemical composition of the as-cast $Co_{68}Al_{18.2}Fe_{6.5}V_{4.75}Cr_{2.55}$ alloy determined by SEM-EDX test was listed in Table 1. The phase structure and chemical composition of the as-cast MEA were characterized by a FEI Talos F200X transmission electron microscope (TEM) at a voltage of 200 kV with an energy-dispersive X-ray spectroscopy (EDS). Electron back-scattered diffraction (EBSD) measurement was conducted on JEOL-JSM-IT800 instruments equipped with an Oxford Symmetry S2 detector. The scanning step size and the scanning area are 0.16 μm and 60 × 60 μm^2, respectively. The nano-indentation tests with the maximum load of 30 mN was conducted on KLA-Nano indenter G200 machine. Rectangular specimens with dimensions of 2 × 2 × 4 mm^3 were cut from the as-cast ingot by electric discharge machine and tested for room-temperature compression and high-temperature compression tests. Room-temperature compression tests were conducted on an Instron 5969 universal testing machine at a strain rate of 2×10^{-4} s^{-1}. High-temperature compression tests of 600 °C and 800 °C were performed on a SUNS-UTM5305H machine equipped with a radial heating furnace at a strain rate of 2×10^{-4} s^{-1}. To obtain reliable test data and ensure the repeatability of the test, at least 3 samples are used for each test.

3. Results

3.1. Phase identification and microstructure of the as-cast MEA

XRD pattern in Fig. 1 for the as-cast $Co_{68}Al_{18.2}Fe_{6.5}V_{4.75}Cr_{2.55}$ MEA shows characteristic peaks of FCC and BCC phases, indicating that the as-cast MEA is a dual-phase microstructure consisting of FCC + BCC constituents. Notably, a superlattice peak is observed at 31°, which is

Table 1
Chemical composition of the as-cast $Co_{68}Al_{18.2}Fe_{6.5}V_{4.75}Cr_{2.55}$ alloy determined by SEM-EDX.

Alloy	Chemical composition (at%)				
	Co	Al	Fe	V	Cr
The studied alloy	68.83	16.69	6.88	4.79	2.81

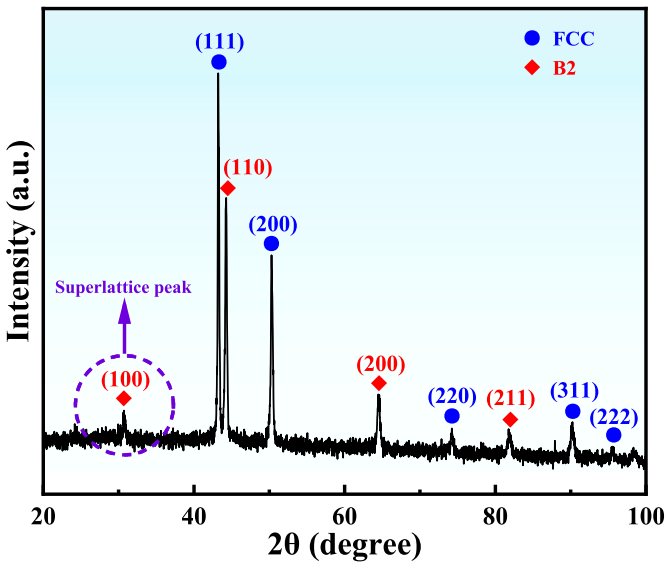

Fig. 1. X-Ray Diffraction pattern for the as-cast $Co_{68}Al_{18.2}Fe_{6.5}V_{4.75}Cr_{2.55}$ dual-phase MEA.

identified as the reflection from (100) plane of the cubic structure, revealing the existence of an ordered cubic (B2) phase. Furthermore, the crystal structure of FCC and B2 phases can be identified. Specifically, the space group of an FCC structure and an ordered B2 structure are $Fm\bar{3}m$ (225) and $Im\bar{3}m$ (229), respectively. Moreover, the lattice parameter of the major FCC phase is 3.545 Å. And the lattice parameter of B2 phase is 2.876 Å. According to the lattice mismatch equation of $\delta = 2(\alpha_{FCC}-\alpha_{B2})/(\alpha_{FCC}+\alpha_{B2})$, the co-existence of FCC matrix and B2 phase exhibits a lattice misfit about 0.2084.

SEM microstructure of the as-cast $Co_{68}Al_{18.2}Fe_{6.5}V_{4.75}Cr_{2.55}$ alloy showed a grain boundary FCC phase and the grain interior (idiomorphic) decorated with FCC and B2 phases exhibiting different morphologies (Fig. 2). It should be noted that the FCC phase exhibited two different morphologies in the current study, i.e., coarse band-like or Widmanstätten-like (Fig. 2(b)) FCC phase formed during solidification and ultrafine vermicular or noodles-like structures formed within the B2 grains.

Fig. 3 exhibits the representative EBSD maps of the as-cast $Co_{68}Al_{18.2}Fe_{6.5}V_{4.75}Cr_{2.55}$ MEA. Fig. 3(a) shows the grain orientation of FCC and B2 structures. Herein, different colors indicate different crystal orientations relative to the surface normal and the orientation relationship (OR) of FCC and B2 structures was established. Based on the EBSD phase map, the volume fractions of FCC and B2 phases are measured to be about 70.3 % and 29.7 %, respectively, as shown in Fig. 3(b). According to Fig. 3 (c), close-packed plane (CCP) and close-packed direction (CCD) have a clear correlation following the Kurdjumov-Sachs (KS) orientation relationship [37,38], and here, one of the poles matches exactly and the remaining poles are slightly off, revealing the semi-coherent relationship between FCC and B2 structures.

Fig. 4 exhibits the microstructure and element distributions of Co, Al, Cr, Fe and V elements in the as-cast dual-phase $Co_{68}Al_{18.2}Fe_{6.5}V_{4.75}Cr_{2.55}$ MEA by scanning transmission electron microscopy (STEM) investigations. The high-angle annular dark field scanning transmission (HAADF) image in Fig. 4(a) shows the detailed dual-phase microstructures consisting of FCC and B2 structures. Fig. 4(b)–(f) exhibits the EDS mapping images, revealing that Co, Fe and Cr are enriched in FCC phase, while Al is enriched in B2 phase. And V is uniformly distributed in FCC and B2 phases. Corresponding chemical composition of FCC phase and B2 phase was determined by TEM-EDX, as listed in Table 2.

In order to further identify the microstructure of the as-cast dual-phase $Co_{68}Al_{18.2}Fe_{6.5}V_{4.75}Cr_{2.55}$ MEA, TEM observation was performed, as shown in Fig. 5. Fig. 5(a) exhibits the bright-field TEM image of the as-cast MEA and alternating dual phases can be clearly observed. The SAED patterns for the dual phases illustrated in Fig. 5(b) and (d) further confirm the FCC phase and B2 phase, which is in agreement with the results of XRD pattern in Fig. 1. Moreover, the characterization of FCC/B2 phases was conducted by high-resolution TEM (HR-TEM), as shown in Fig. 5(c) and (e). The fast Fourier transformation patterns in the upper right corner of Fig. 5(c) and (e) further verify the microstructure of the two phases. To determine the relationship of dual phases, the HR-TEM image of the inter-phase interface between the FCC and B2 phases is shown in Fig. 5(g) and the interface is rough at atomic scale. Furthermore, the Fast Fourier transformation (FFT) for the identical inter-phase region marked in Fig. 5(g), in which the diffraction spots connected by the red and yellow dotted line are the [100] and [101] crystal zone axis of the FCC and B2 phases, respectively. Note that the (1,1,-1) spot of the FCC phase coincide with the (0,1,1) spot of the B2 phase in Fig. 5(h). Hence, the orientation relationship between the two phases is determined to be $[11\text{-}1]_{FCC} \parallel [011]_{B2}$, following the classical Kurdjumov-Sachs (KS) relationship [37,38], which is consistent with the results of the pole figure analysis of FCC and B2 phases in Fig. 3(c). Fig. 5(i) exhibits the relevant inverse FFT (IFFT) image of the identical inter-phase region and a semi-coherent interface can be observed, accompanied with many lattice misfit dislocations.

3.2. *Mechanical properties of the as-cast dual-phase MEA*

In order to better understand the intrinsic essence of FCC and B2 phases, the nanoindentation tests was conducted, as shown in Fig. 6. The load-displacement curves (Fig. 6(a)) indicate that FCC phase shows a larger maximum indentation depth (h_{max}) than that of B2 phase, which

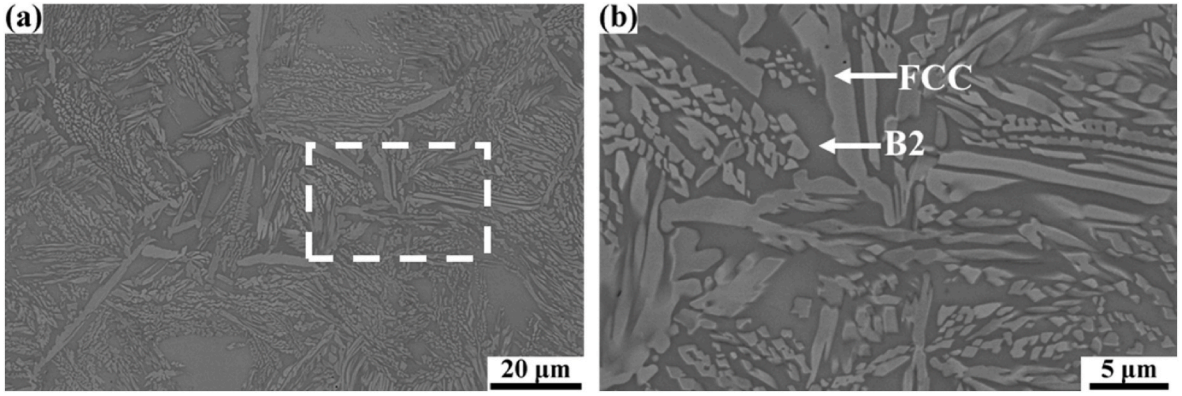

Fig. 2. (a) SEM images of the as-cast $Co_{68}Al_{18.2}Fe_{6.5}V_{4.75}Cr_{2.55}$ MEA. (b) High-magnification SEM image of the region in white rectangle in (a).

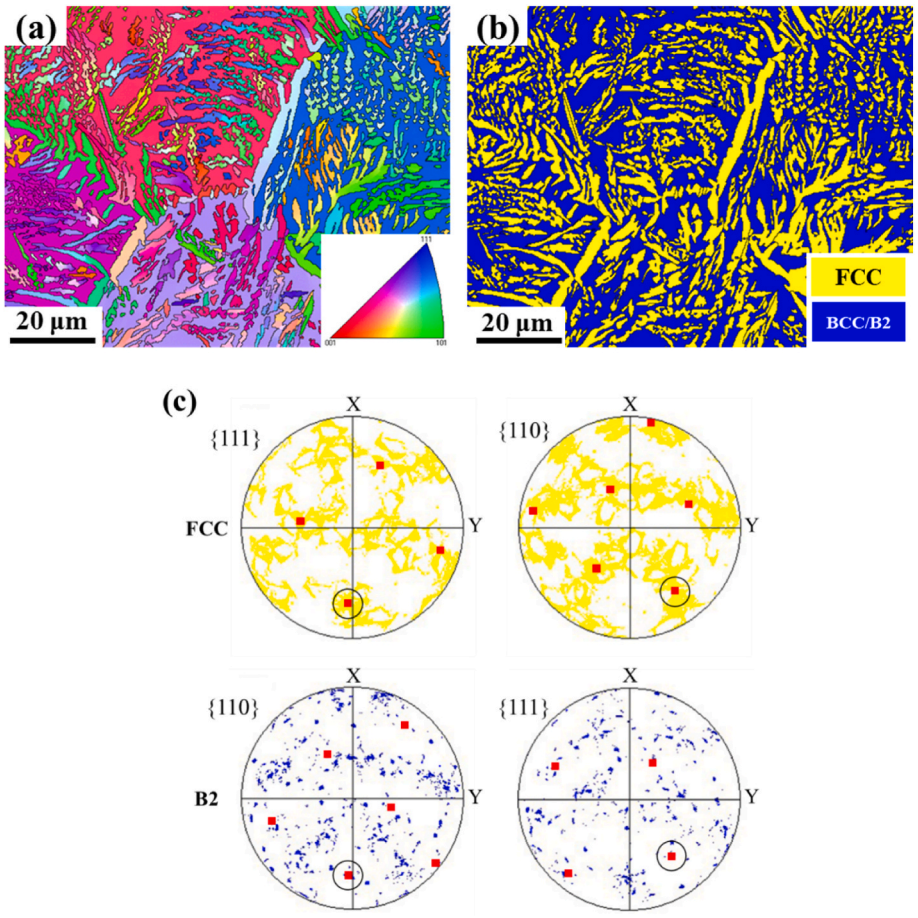

Fig. 3. EBSD maps of the as-cast dual-phase MEA. (a) Grain orientation map of FCC and B2 structures. (b) Phase map pf the as-cast MEA revealing the presence of FCC (yellow) and B2 (blue) phases. (c) Pole figure analysis of FCC (yellow) and B2 (blue) phases.

are 410 nm and 354 nm, respectively. Meanwhile, both the hardness and modulus of B2 phase is larger than that of FCC phase, as shown in Fig. 6 (b).

To reveal the effect of dual-phase microstructure on the mechanical properties of the as-cast $Co_{68}Al_{18.2}Fe_{6.5}V_{4.75}Cr_{2.55}$ MEA, compression tests under room temperature (RT) and high temperature (HT) of 600 and 800 °C were carried out. Fig. 7 shows the compressive engineering stress-strain curves of the as-cast MEA at RT and HT, where the compressive yield strength, fracture strength and fracture strain of the as-cast MEA at RT are 1254 MPa, 2657 MPa and 34.6 %, respectively, indicating that the as-cast MEA possesses both high strength and large plasticity. Moreover, the compressive yield strength of the as-cast MEA at 600 °C and 800 °C are 1213 MPa and 626 MPa, respectively. The comparison of the compressive performance of the as-cast MEA at RT and HT with that of some common HEAs/MEAs and commercial alloys reported in literatures [39–57] is shown in Fig. 8. Fig. 8(a) indicates that the as-cast MEA exhibits excellent compressive mechanical properties at RT compared with some reported MEAs and commercial alloys, while Fig. 8(b) displays that the as-cast MEA exhibits superior high-temperature performance. For example, the compressive yield strength of the as-cast MEA at 600 °C is 1213 MPa, which is slightly lower than that of at RT. Similarly, the as-cast MEA exhibits a high yield strength of 626 MPa at 800 °C. Therefore, the as-cast MEA designed in this work not only exhibits the synergy of high yield strength and large plasticity, but also embraces distinguished high-temperature mechanical properties over a wide temperature range, possessing a promising potential for practical engineering applications at elevated temperatures.

For a better understanding of the fracture behavior and mechanism of the as-cast $Co_{68}Al_{18.2}Fe_{6.5}V_{4.75}Cr_{2.55}$ MEA at room temperature, the representative fracture morphology of the as-cast MEA after room-temperature compression was presented in Fig. 9. Fig. 9(a) shows the low-magnification fracture morphology of the as-cast MEA and both ductile and brittle characteristics can be observed simultaneously. For example, river-like patterns, flat surface and dimples appear simultaneously on the fracture surface (Fig. 9(b)) [61,62]. Similarly, Fig. 9(c) shows the laminar and dimple fracture features, which indicates the coexistence of ductile fracture and brittle fracture [63]. Specifically, it can be inferred from Fig. 9(d) that the rough lamellar features containing dimples are derived from the soft FCC phase, while the smooth lamellar features are derived from the hard B2 phase.

4. Discussion

4.1. Phase formation

The prediction of phase formation is vital for the composition design of MEAs. To predict the phase formation, some empirical parameters were proposed [63–67], such as the atomic size difference (δ), the mixing entropy (ΔH_{mix}), the mixing enthalpy (ΔS_{mix}), average valence electron concentration (VEC), the relationship between mixing entropy and enthalpy (Ω) and the electronegativity difference ($\Delta\chi$), which were defined by Eqs. (1)–(6), respectively.

$$\Delta H_{mix} = \sum_{i=1,i\neq j}^{n} \Omega_{ij} c_i c_j = \sum_{i=1,i\neq j}^{n} 4\Delta H_{ij}^{mix} c_i c_j \quad (1)$$

where n is the number of elements in the alloy. c_i and c_j are the atomic

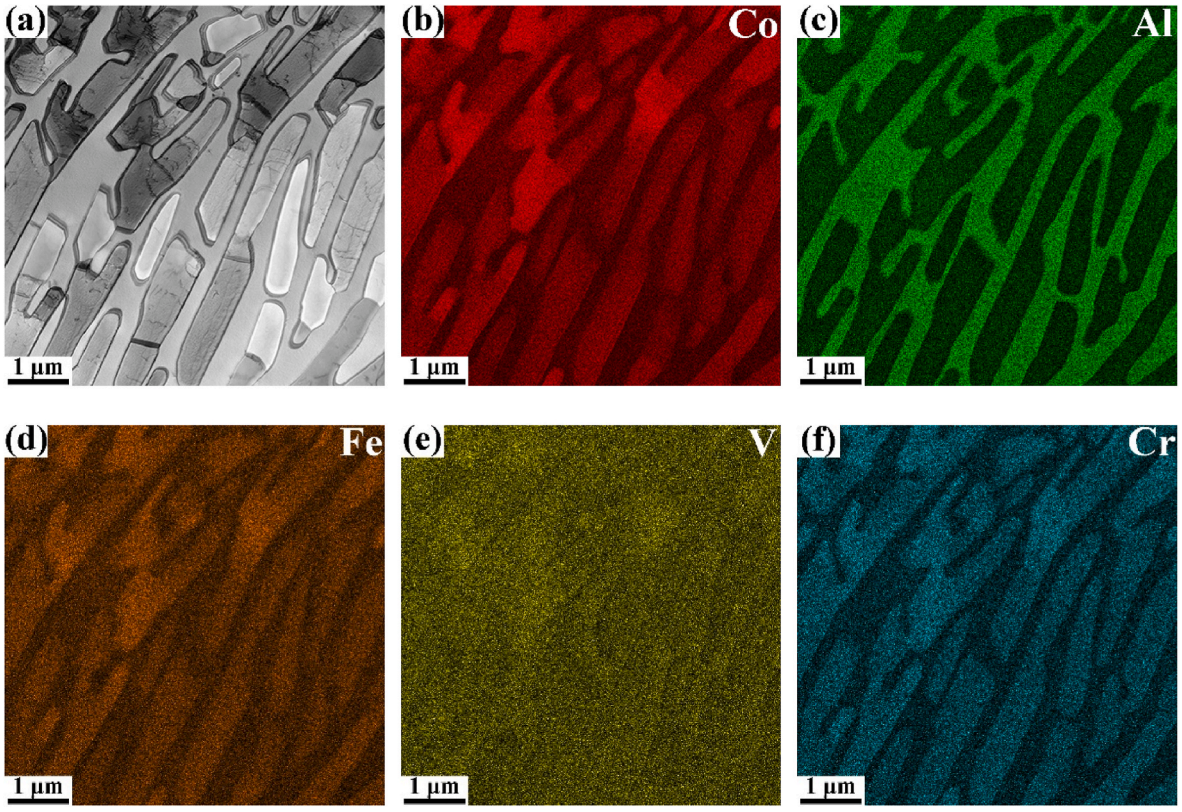

Fig. 4. High-angle annular dark-field (HAADF) and STEM-EDS mapping images of the as-cast dual-phase $Co_{68}Al_{18.2}Fe_{6.5}V_{4.75}Cr_{2.55}$ MEA. (a) HAADF image. (b)–(f) Elemental distribution maps of Co, Al, Fe, V, Cr, respectively.

Table 2
Chemical composition of FCC phase and B2 phase the as-cast $Co_{68}Al_{18.2}Fe_{6.5}V_{4.75}Cr_{2.55}$ alloy detected by TEM-EDX.

Phases	Chemical composition (at%)				
	Co	Al	Fe	V	Cr
FCC	74.15	10.53	7.75	4.32	3.25
B2	66.73	19.16	6.71	5.22	2.18

percent of the ith and jth elements, respectively. ΔH_{ij}^{mix} is the mixing enthalpy between the i_{th} and j_{th} elements.

$$\Delta S_{mix} = R\sum_{i=1}^{n} c_i \ln c_i \quad (2)$$

where R is the gas constant (8.314 J K ^{1} mol ^{1}).

$$VEC = \sum_{i=1}^{n} c_i (VEC)_i \quad (3)$$

where $(VEC)_i$ is the valence electron concentration for the ith element.

$$\delta = \sqrt{\sum_{i=1}^{n} c_i \left(1 \quad \frac{r_i}{\bar{r}}\right)^2}, \bar{r} = \sum_{i=1}^{n} c_i r_i \quad (4)$$

where r_i and $\bar{r}$ are the atomic radius of ith element and the average atomic radius of the alloy elements, respectively.

$$\Omega = \frac{T_m \Delta S_{mix}}{|\Delta H_{mix}|}, T_m = \sum_{i=1}^{n} c_i (T_m)_i \quad (5)$$

where $(T_m)_i$ the melting point of the ith element.

$$\Delta\chi = \sqrt{\sum_{i=1}^{n} c_i (\chi_i \quad \bar{\chi})^2} \quad (6)$$

where $\bar{\chi} = \sum_{i=1}^{n} c_i \chi_i$, And χ_i is the Pauling electronegativity for the ith element.

According to Eqs. (1)–(6), the ΔH_{mix}, ΔS_{mix}, VEC, δ, Ω and $\Delta\chi$ of the studied alloy can be calculated, as listed in Table 3.

Based on the above thermodynamic parameters, some empirical rules of phase prediction have also been proposed. For example, Guo et al. proposed that BCC phase is stable when VEC ≥8.0, BCC phase is stable when VEC ≤6.87, while FCC and BCC phases coexist when 6.87 < VEC < 8 [17]. Moreover, the δ-ΔH_{mix} model was proposed to predict the formation of solid solution phase, i.e., when δ < 6.6 % and 11.6 < ΔH_{mix} < 3.2 kJ/mol, the simple solid-solution phase is formed [68]. Meanwhile, the δ-Ω model can be used to predict the formation of solid solution phase, i.e., when Ω ≥ 1.1 and δ ≤ 6.6 %, the solid solution phase is formed [64]. Generally, the alloy tends to form an MEA when 0.69R ≤ ΔS_{mix} ≤ 1.61R, which have been widely used and highly recognized [69, 70].

According to the calculated thermodynamic parameters of the studied alloy illustrated in Table 2, the δ and ΔH_{mix} of the as-designed MEA are 5.48 % and 13.03 kJ mol ^{1}, respectively. Fig. 10(a) exhibits the comparison between ΔH_{mix} and δ for the as-designed MEA and other HEAs/MEAs systems, indicating the emergence of multiphase in the as-cast alloy. Moreover, Fig. 10(b) shows the relationship between VEC and the FCC/B2 phases stability for the as-designed HEA and other HEAs/MEAs systems. It can be found that the calculated VEC of the studied alloy is exactly between 6.87 and 8, revealing the formation of dual-phase [17]. The calculated phase diagram from CALPHAD Fig. 11 indicates that the primary B2 phase solidifies from the liquid at 1380 °C. Subsequently, at about 1350 °C, the FCC phase precipitates from the liquid. Therefore, on the basis of these thermodynamic parameters and

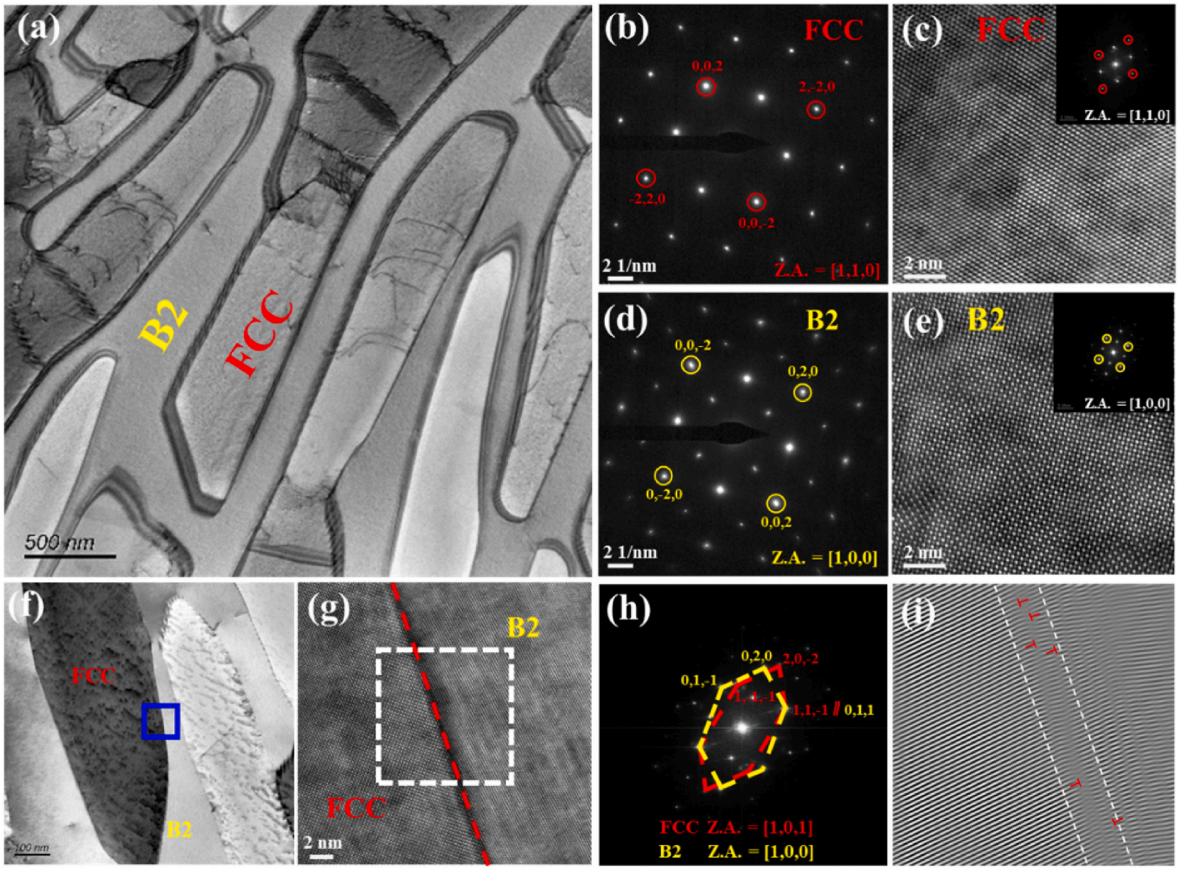

Fig. 5. TEM images of the as-cast dual-phase $Co_{68}Al_{18.2}Fe_{6.5}V_{4.75}Cr_{2.55}$ MEA. (a) TEM-BF microstructure of the as-cast dual-phase MEA. (b) Selected-area electron diffraction (SAED) pattern of FCC phase. (c) HR-TEM image of FCC phase. The inset is SAED pattern of FCC structure with the zone [1,1,0] axis. (d) SAED pattern of B2 phase. (e) HR-TEM image of B2 phase. The inset is SAED pattern of B2 structure with the zone [1,0,0] axis. (f) The interface between FCC and B2 phases. (g) HR-TEM image of FCC/B2 phase interfaces from the region marked in blue in (f). (h) The Fast Fourier transformation (FFT) for the interface between FCC and B2 phases marked in (f). (i) The inverse fast-Fourier-transformed (IFFT) images of the HR-TEM image of area marked by a blue box in (f) (symbol "⊥" means a dislocation).

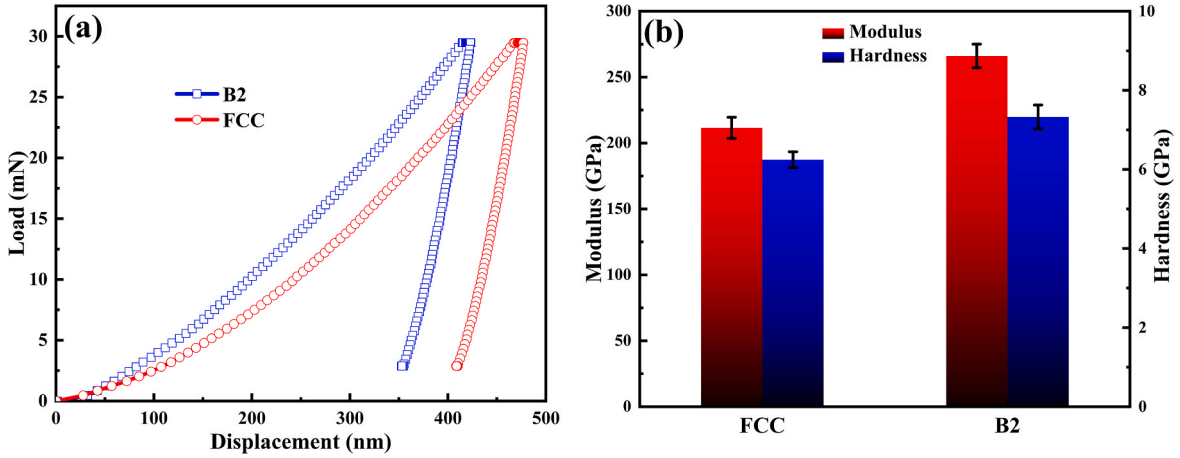

Fig. 6. (a) Load-displacement graph obtained from nanoindentation test for FCC and B2 phases. (b) Comparison of hardness and modulus of FCC and B2 phases.

calculated phase diagram, it can be concluded that the formation of FCC and B2 phases in the as-designed $Co_{68}Al_{18.2}Fe_{6.5}V_{4.75}Cr_{2.55}$ alloy correlates well with the partial phase diagram showing that only stable phases formed during the solidification process.

4.2. *Strengthening mechanism*

The mechanical properties of MEAs are closely related to their phase composition and microstructure [76]. For the as-cast MEA, its excellent comprehensive mechanical properties at room temperature and high temperature (Fig. 7(a) and (b)) is attributed to the cooperative deformation of the soft FCC and hard B2 phases. During deformation, after the soft FCC and hard B2 phases co-deformed elastically, plastic deformation would occur firstly in the soft FCC phase. And yet the soft FCC phase matrix cannot undergo plastic deformation freely due to the constraint by the surrounding hard B2 phase [77]. In order to maintain the strain

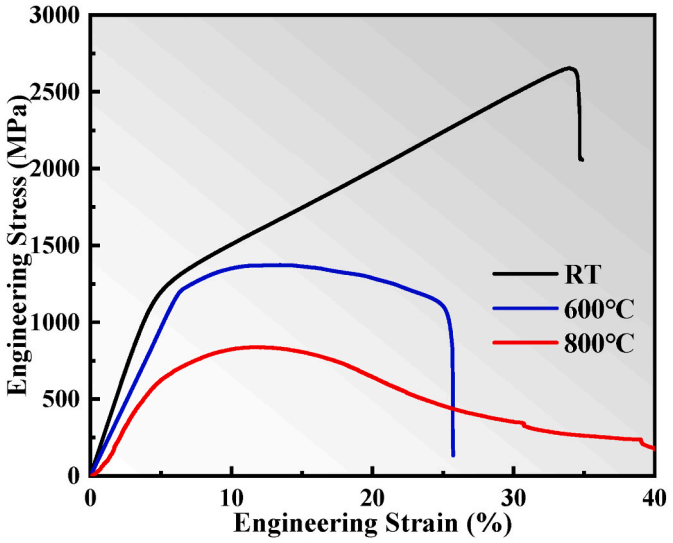

Fig. 7. Mechanical performance of the as-cast $Co_{68}Al_{18.2}Fe_{6.5}V_{4.75}Cr_{2.55}$ MEA under compression tests at room temperature and high temperature of 600 and 800 °C.

continuity, the plastic-strain gradients exist in the soft FCC matrix near interfaces, leading to the storage of geometrically necessary dislocations [78]. Thus, a long-range back-stress generated in this process, making dislocations difficult to move in soft FCC matrix until hard B2 phase begin to yield deformation [79]. Moreover, some coarse FCC grains is simultaneously surrounded by the intergranular B2 phase, resulting in the occurrence of the same back-stress [80]. Therefore, under the constraint of hard B2 grains, the FCC grains seem to be much stronger, generating so-called synergetic strengthening and significantly increasing the yield strength [81]. After yielding, both the soft FCC and hard B2 phase will deformation plastically. However, the FCC matrix undergoes more plastic strain than hard BCC matrix, causing the occurrence of further strain gradients. At this point, the strain gradients exist in both FCC and BCC matrix, further elevating the strain gradients and requiring more geometrically necessary dislocations [81]. And the back-stress hardening is further enhanced. Based on this theory, such strain gradients and back-stress hardening will significantly contribute to the observed high strength and large ductility together [82]. In addition, semi-coherent orientation relationship between FCC phase and B2 phase (Fig. 5(i)) hinders the dislocation slip, further enhancing the strength of the as-cast MEA. Meanwhile, the as-cast MEA shows a large compressive plasticity of 34.6 %, which is ascribed to a high-volume fraction of soft FCC phase (70.3 %) with high number of slip planes. Therefore, the proper combination of FCC and B2 phases in MEA can obtain outstanding mechanical properties, effectively breaking the trade-off of strength and plasticity. In particular, as the test temperature increases from room temperature to 600 °C, the yield strength of the as-cast MEA does not decrease significantly, which indicates that the as-cast MEA has high thermal stability and high-temperature strength. Superior high-temperature performance of the as-cast MEA is mainly attributed to the existence of ordered B2 phase. It is well known that B2 phase retain nearly constant strength level at temperatures from room temperature to about ~0.4 T_m (melting temperature), while an obvious decrease of yield strength occurs at higher temperatures [83,84]. According to the calculated phase diagram (Fig. 10), the value of 0.4T_m of the as-designed MEA can be estimated as ~552 °C, which is associated well with the observed preservation of high strength at temperatures up to 600 °C (Fig. 7(b)). The existence of B2 phase effectively suppresses the nucleation and propagation of microcracks, contributing to high strength and ductility at high temperature [85,86]. When the test temperature is 800 °C, the yield strength of the as-cast MEA is reduced to 626 MPa, outperforming most HEAs and some commercial alloys (Fig. 8 (b)). This is attributed to that the strain energy stored between FCC and B2 phases in the process of deformation provides the driving force for dynamic recovery and recrystallization at higher temperatures due to the difference in hardness of the two constituent phases [87,88]. In addition, compared with the compression ductility at room temperature, the studied MEA tested at 600 °C exhibits a reduced ductility, which may be due to lowered strain hardening rate, grain boundary embrittlement and dynamic-strain aging induced stress instability [89–92]. Specifically, the studied alloys may undergo aging treatment and oxygen tends to invade the grain boundary during the compression tests at 600 °C, triggering the formation some brittle phases. At higher temperature (e.g., 800 °C), the continuous dynamic recrystallization and dislocation annihilation effectively relieve stress concentration and prevent microcrack formation at grain boundaries, thus the studied MEA deforms more easily and strain become softening [93,94]. Corresponding deformation mechanism at the high temperature will be studied more detailly in future work.

5. Conclusions

In conclusion, we designed a novel dual-phase $Co_{68}Al_{18.2}Fe_{6.5}V_{4.75}Cr_{2.55}$ MEA with FCC + B2 structure, which not only exhibits an excellent strength-ductility combination at room temperature, but also presents an outstanding high-temperature mechanical properties in

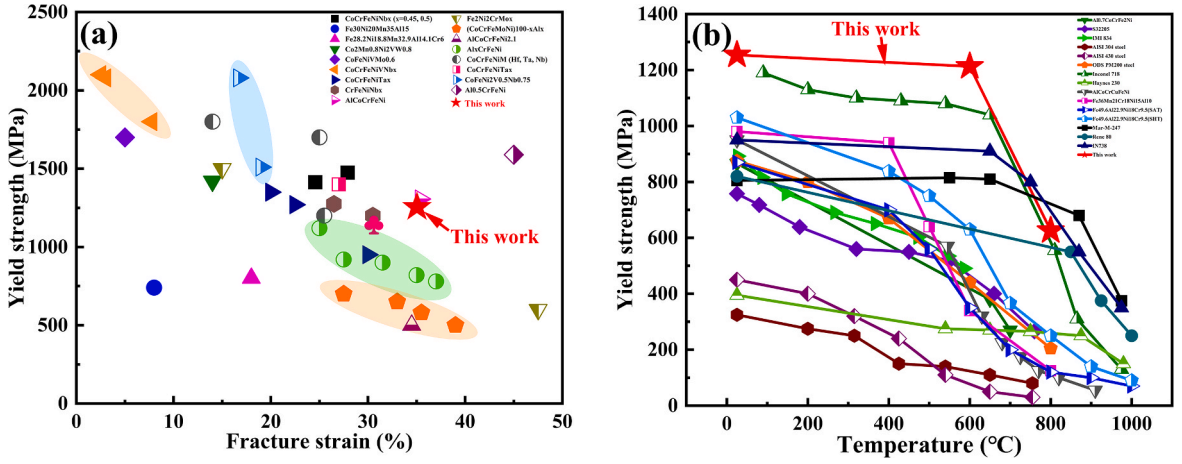

Fig. 8. (a) Yield strength versus fracture strain of the as-cast $Co_{68}Al_{18.2}Fe_{6.5}V_{4.75}Cr_{2.55}$ MEA in comparison with some common MEAs and commercial alloys [39–55]. (b) Comparison between yield strength of the as-cast MEA and some common HEAs/MEAs and commercial alloys as a function of temperature [56–60].

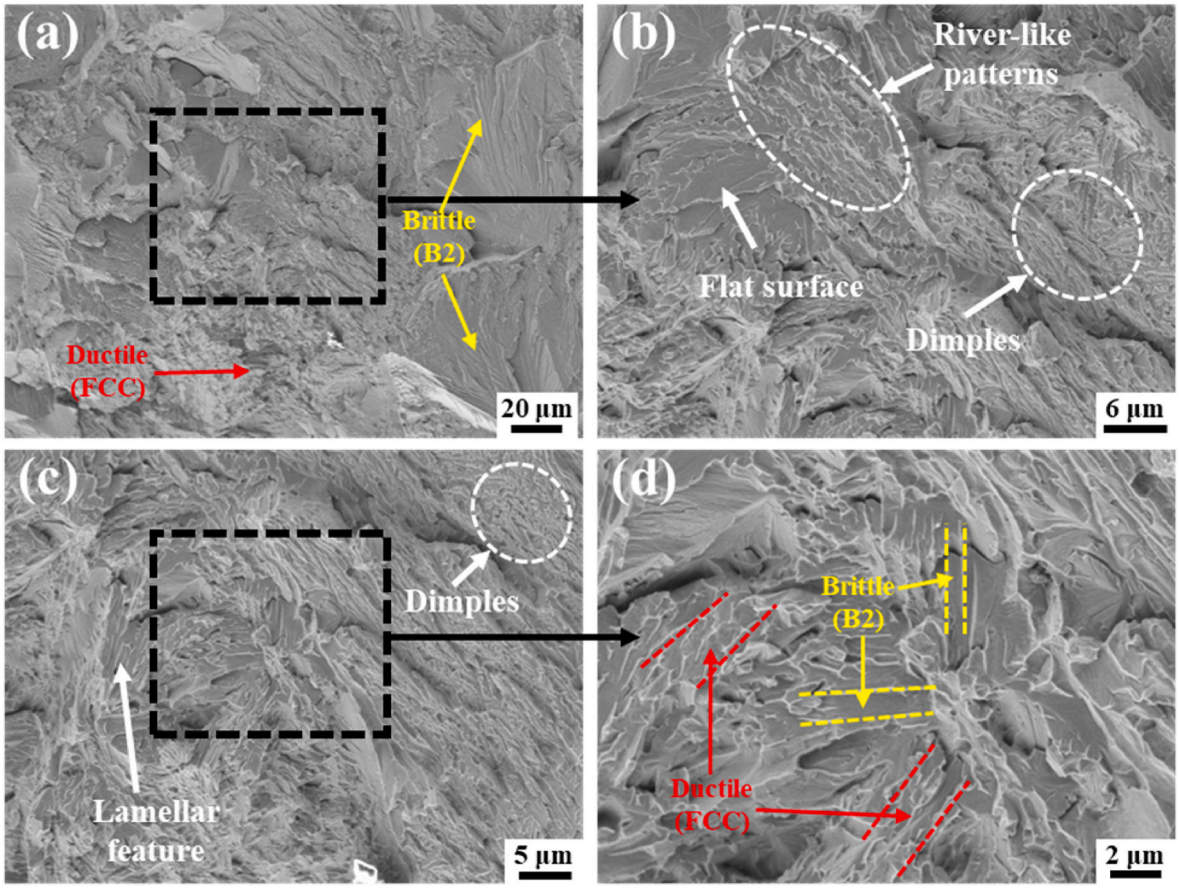

Fig. 9. (a) and (c) Representative fracture morphologies of the as-cast $Co_{68}Al_{18.2}Fe_{6.5}V_{4.75}Cr_{2.55}$ HEA after room-temperature compression. (b) and (d) are the high-magnification images marked in black dotted box in (a) and (c), respectively.

Table 3
The calculated thermodynamic parameters of the studied $Co_{68}Al_{18.2}Fe_{6.5}V_{4.75}Cr_{2.55}$ MEA.

Alloy	ΔH_{mix} kJ·mol ^{1}	ΔS_{mix} J·K ^{1}·mol ^{1}	VEC	δ %	Ω	$\Delta\chi$	T_m K
$Co_{68}Al_{18.2}Fe_{6.5}V_{4.75}Cr_{2.55}$	13.03	8.22	7.58	5.48	1.04	0.11	1647

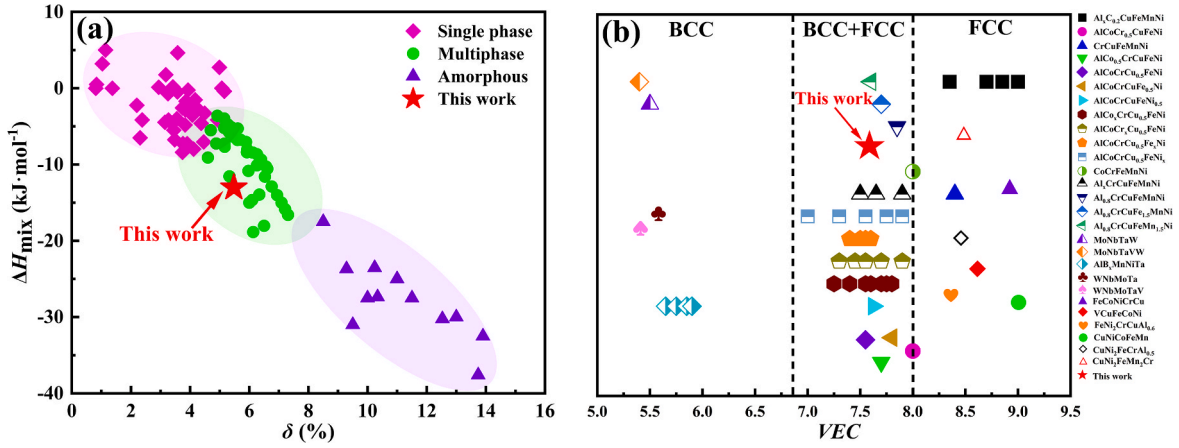

Fig. 10. (a) Comparison between ΔH_{mix} and δ for the as-designed $Co_{68}Al_{18.2}Fe_{6.5}V_{4.75}Cr_{2.55}$ MEA and other HEAs/MEAs systems [71]. (b) Relationship between VEC and the FCC/BCC phases stability for the as-designed HEA and other HEA systems [72–75].

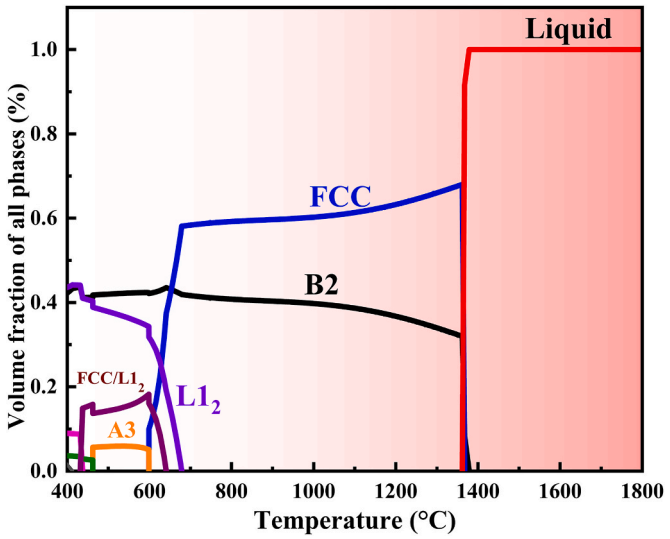

Fig. 11. Calculated phase volume fraction plot of $Co_{68}Al_{18.2}Fe_{6.5}V_{4.75}Cr_{2.55}$ alloy as a function of temperature based on CALPHAD.

particular. The phase formation, microstructure and mechanical behaviors of the designed dual-phase MEA at room and high temperatures were investigated and discusses systematically. In detail, the newly designed MEA shows a dual-phase structure containing FCC phase (70.3 vol %) plus B2 phase (29.7 vol %), which is demonstrated by experimental methods (XRD, SEM and TEM) and theoretical analysis (calculated diagram and empirical thermodynamic parameters). The FCC phase is enriched with Co, Fe and Cr elements, while the B2 phase is enriched with Al element. And V is uniformly distributed in FCC and B2 phases. Furthermore, the as-designed MEA shows excellent comprehensive mechanical properties with a high compressive yield strength of ~1254 MPa, a fracture strength of ~2657 MPa and a large compressive plasticity of ~34.6 % at room temperature. In particular, an ultrahigh yield strength of ~1213 MPa at 600 °C and 626 MPa at 800 °C can be obtained in this studied MEA. The outstanding mechanical performance of this designed MEA at both room and temperatures mainly originate from synergy effect of alternate FCC + B2 structure and strengthening contributions of B2 phase. These important findings not only reveal the deformation and strengthening mechanisms of dual-phase MEA, but also provides an effective alloy design strategy for developing advanced structural materials serving as a wide range of temperature.

CRediT authorship contribution statement

Xiangkui Liu: Writing – review & editing, Writing – original draft, Methodology, Formal analysis, Data curation, Conceptualization. **Shuai Feng:** Formal analysis, Data curation, Conceptualization. **Huiqing Xu:** Data curation, Conceptualization. **Conghao Liu:** Data curation, Conceptualization. **Xulong An:** Data curation, Conceptualization. **Zhuqi Chu:** Data curation, Conceptualization. **Wei Wei:** Data curation, Conceptualization. **Dandan Wang:** Data curation, Conceptualization. **Yemao Lu:** Data curation, Conceptualization. **Zhenfei Jiang:** Visualization, Validation, Formal analysis, Data curation, Conceptualization. **Jian Kong:** Investigation, Formal analysis, Data curation, Conceptualization.

Declaration of competing interest

The authors declare that they have no known competing financial interests or personal relationships that could have appeared to influence the work reported in this paper.

Data availability

Data will be made available on request.

Acknowledgment

This work was supported by Key Laboratory of Surface Engineering and Advanced Materials for Petroleum and Chemical Industry (Changzhou University) (No. 22SEAM001), and supported by Sinoma Institute of Materials Research (Guang Zhou) Co., Ltd (SIMR) for assisting the TEM/SEM characterization. Xulong An gratefully acknowledges the support of Natural Science Foundation for Young Scholars of Jiangsu Province (Grant No. BK20220628) and National Natural Science Foundation for Young Scholars of China (52301130). Dandan Wang gratefully acknowledges the support of Natural Science Foundation of Jiangsu Provincial Education Department (No. 21KJB430001).

References

[1] D. Raabe, C.C. Tasan, E.A. Olivetti, Strategies for improving the sustainability of structural metals, Nature 575 (2019) 64–74, https://doi.org/10.1038/s41586-019-1702-5.
[2] G.D. Sim, J.A. Krogstad, K.M. Reddy, K.Y. Xie, G.M. Valentino, T.P. Weihs, K. J. Hemker, Nanotwinned metal MEMS films with unprecedented strength and stability, Sci. Adv. 3 (2017) 1700685, https://doi.org/10.1126/sciadv.1700685.
[3] Y. Xie, C. Wang, K. Zhang, C. Liang, M. Liang, W. Liu, J. Yang, Microstructure transformation and high temperature oxidation properties of $(FeCoNi)_{100-x}Al_x$ new-type high-entropy alloys, Vacuum 191 (2021) 110364, https://doi.org/10.1016/j.vacuum.2021.110364.
[4] J.W. Yeh, S.K. Chen, S.J. Lin, J.Y. Gan, T.S. Chin, T.T. Shun, C.H. Tsau, S.Y. Chang, Nanostructured high-entropy alloys with multiple principal elements: novel alloy design concepts and outcomes, Adv. Eng. Mater. 6 (2004) 299–303, https://doi.org/10.1002/adem.200300567.
[5] B. Cantor, I.T.H. Chang, P. Knight, A.J.B. Vincent, Microstructural development in equiatomic multicomponent alloys, Mater. Sci. Eng. 375–377 (2004) 213–218, https://doi.org/10.1016/j.msea.2003.10.257.
[6] X.S. Liu, M.D. Zhang, Y.M. Ma, W.Q. Dong, R. Li, Y. Lu, Y.F. Zhang, P.F. Yu, Y. P. Gao, G. Li, Achieving ultrahigh strength in CoCrNi-based medium-entropy alloys with synergistic strengthening effect, Mater. Sci. Eng. 776 (2020) 139028, https://doi.org/10.1016/j.msea.2020.139028.
[7] J.T. Fan, L.J. Zhang, G. Li, R.P. Liu, A novel high-entropy alloy with dendrite composite microstructure and remarkable compression performance, Scripta Mater. 159 (2019) 18–23, https://doi.org/10.1016/j.scriptamat.2018.09.008.
[8] D. Yang, Y. Liu, H. Jiang, M. Liao, N. Qu, T. Han, Z. Lai, J. Zhu, A novel FeCrNiAlTi-based high entropy alloy strengthened by refined grains, J. Alloys Compd. 823 (2020) 153729, https://doi.org/10.1016/j.jallcom.2020.153729.
[9] Y.B. Peng, W. Zhang, X.L. Mei, H.J. Wang, M.Y. Zhang, L. Wang, X.F. Li, Y. Hu, Microstructures and mechanical properties of FeCoCrNi-Mo High entropy alloys prepared by spark plasma sintering and vacuum hot-pressed sintering, Mater. Today Commun. 24 (2020) 101009, https://doi.org/10.1016/j.mtcomm.2020.101009.
[10] C.P. Lee, C.C. Chang, Y.Y. Chen, J.W. Yeh, H.C. Shih, Effect of the aluminium content of AlxCrFe1.5MnNi0.5 high-entropy alloys on the corrosion behaviour in aqueous environments, Corrosion Sci. 50 (2008) 2053–2060, https://doi.org/10.1016/j.corsci.2008.04.011.
[11] O.N. Senkov, S.V. Senkova, C. Woodward, Effect of aluminum on the microstructure and properties of two refractory high-entropy alloys, Acta Mater. 68 (2014) 214–228, https://doi.org/10.1016/j.actamat.2014.01.029.
[12] F. Otto, A. Dlouhý, C. Somsen, H. Bei, G. Eggeler, E.P. George, The influences of temperature and microstructure on the tensile properties of a CoCrFeMnNi high entropy alloy, Acta Mater. 61 (2013) 5743–5755, https://doi.org/10.1016/j.actamat.2013.06.018.
[13] Y.P. Lu, Y. D, S. Guo, L. Jiang, H.J. Kang, T.M. Wang, B. Wen, Z.J. Wang, J.C. Jie, Z. Q. Cao, H.H. Ruan, T.J. Li, A promising new class of high temperature alloys: eutectic high-entropy alloys, Sci. Rep. 4 (2014) 6200, https://doi.org/10.1038/srep06200.
[14] Z.M. Li, K.G. Pradeep, Y. Deng, D. Raabe, C.C. Tasan, Metastable high-entropy dual-phase alloys overcome the strength-ductility trade off, Nature 534 (2016) 227–230, https://doi.org/10.1038/nature17981.
[15] P. Shi, W. Ren, T. Zheng, Z. Ren, X. Hou, J. Peng, P. Hu, Y. Gao, Y. Zhong, P. K. Liaw, Enhanced strength-ductility synergy in ultrafine-grained eutectic high-entropy alloys by inheriting microstructural lamellae, Nat. Commun. 10 (2019) 489–497, https://doi.org/10.1038/s41467-019-08460-2.
[16] P. Shi, Y. Zhong, Y. Li, W. Ren, Y. Zhu, Multistage work hardening assisted by multi-type twinning in ultrafine-grained heterostructural eutectic high-entropy alloys, Mater. Today 41 (2020) 62–71, https://doi.org/10.1016/j.mattod.2020.09.029.

[17] G. Sheng, C. Ng, L. Jian, C.T. Liu, Effect of valence electron concentration on stability of fcc or bcc phase in high entropy alloys, J. Appl. Phys. 109 (2011) 103505, https://doi.org/10.1063/1.3587228.

[18] W. Lu, X. Luo, Y. Yang, J. Zhang, B. Huang, Effects of Al addition on structural evolution and mechanical properties of the CrCoNi medium-entropy alloy, Mater. Chem. Phys. 238 (2019) 121841, https://doi.org/10.1016/j.matchemphys.2019.121841.

[19] L.J. Lin, X. Xian, Z.H. Zhong, Y.C. Wu, P.K. Liaw, Microstructure stability and its influence on the mechanical properties of CrMnFeCoNiAl0.25 high entropy alloy, Met. Mater. Int. 26 (2019) 1192–1199, https://doi.org/10.1007/s12540-019-00542-6.

[20] Y.P. Lu, H. Jiang, S. Guo, T.M. Wang, Z.Q. Cao, T.J. Li, A new strategy to design eutectic high-entropy alloys using mixing enthalpy, Intermetallics 91 (2017) 124–128, https://doi.org/10.1016/j.intermet.2017.09.001.

[21] H. Jiang, K. Han, X.X. Gao, Y.P. Lu, Z.Q. Cao, M.C. Gao, J.A. Hawk, T.J. Li, A new strategy to design eutectic high-entropy alloys using simple mixture method, Mater. Des. 142 (2018) 101–105, https://doi.org/10.1016/j.matdes.2018.01.025.

[22] Y.P. Lu, Y. Dong, H. Jiang, Z.J. Wang, Z.Q. Cao, S. Guo, T.M. Wang, T.J. Li, P. K. Liaw, Promising properties and future trend of eutectic high entropy alloys, Scripta Mater. 187 (2020) 202–209, https://doi.org/10.1016/j.scriptamat.2020.06.022.

[23] F. He, Z.J. Wang, P. Cheng, Q. Wang, J.J. Li, Y.Y. Dang, J.C. Wang, C.T. Liu, Designing eutectic high entropy alloys of CoCrFeNiNbx, J. Alloys Compd. 656 (2016) 284–289, https://doi.org/10.1016/j.jallcom.2015.09.153.

[24] S. Gorsse, D.B. Miracle, O.N. Senkov, Mapping the world of complex concentrated alloys, Acta Mater. 135 (2017) 177–187, https://doi.org/10.1016/j.actamat.2017.06.027.

[25] S. Praveen, H.S. Kim, High-entropy alloys: potential candidates for high-temperature applications-an overview, Adv. Eng. Mater. 20 (2018) 1700645, https://doi.org/10.1002/adem.201700645.

[26] J. Chen, X. Zhou, W. Wang, B. Liu, Y. Lv, W. Yang, D. Xu, Y. Liu, A review on fundamental of high entropy alloys with promising high-temperature properties, J. Alloys Compd. 760 (2018) 15–30, https://doi.org/10.1016/j.jallcom.2018.05.067.

[27] J. Sato, T. Omori, K. Oikawa, I. Ohnuma, R. Kainuma, K. Ishida, Cobalt-base high-temperature alloys, Science 312 (2006) 90–91, https://doi.org/10.1126/science.1121738.

[28] A. Suzuki, G.C. DeNolf, T.M. Pollock, Flow stress anomalies in γ/γ' two-phase Co-Al-W-base alloys, Scripta Mater. 56 (2007) 385–388, https://doi.org/10.1016/j.scriptamat.2006.10.039.

[29] D.B. Miracle, High entropy alloys and their development as structural materials, Mater. Sci. Technol. 31 (2015) 1142–1147, https://doi.org/10.1179/1743284714Y.0000000749.

[30] O.N. Senkov, J.D. Miller, D.B. Miracle, C. Woodward, Accelerated exploration of multi-principal element alloys with solid solution phases, Nat. Commun. 6 (2015) 6529, https://doi.org/10.1038/ncomms7529.

[31] T.M. Pollock, S. Tin, Nickel-based superalloys for advanced turbine engines: chemistry, microstructure and properties, J. Propul. Power 22 (2006) 361–374, https://doi.org/10.2514/1.18239.

[32] A. Manzoni, S. Haas, H. Daoud, U. Glatzel, C. Förster, N. Wanderka, A.M. Manzoni, S. Haas, H. Daoud, U. Glatzel, C. Förster, N. Wanderka, Tensile behavior and evolution of the phases in the $Al_{10}Co_{25}Cr_8Fe_{15}Ni_{36}Ti_6$ compositionally complex high entropy alloy, Entropy 20 (2018) 646, https://doi.org/10.3390/e20090646.

[33] T.K. Tsao, A.C. Yeh, C.M. Kuo, H. Murakami, On the superior high temperature hardness of precipitation strengthened high entropy Ni-based alloys, Adv. Eng. Mater. 19 (2017) 1600475, https://doi.org/10.1002/adem.201600475.

[34] J. Chen, X.Y. Zhou, W.L. Wang, B. Liu, Y.K. Lv, W. Yang, D.P. Xu, Y. Liu, A review on fundamental of high entropy alloys with promising high-temperature properties, J. Alloys Compd. 760 (2018) 15–30, https://doi.org/10.1016/j.jallcom.2018.05.067.

[35] Q. Wang, Y. Ma, B. Jiang, X. Li, Y. Shi, C. Dong, P.K. Liaw, A cuboidal B2 nanoprecipitation- enhanced body-centered-cubic alloy Al0.7CoCrFe2Ni with prominent tensile properties, Scripta Mater. 120 (2016) 85–89, https://doi.org/10.1016/j.scriptamat.2016.04.014.

[36] Y. Zhou, X. Jin, L. Zhang, X. Du, B. Li, A hierarchical nanostructured $Fe_{34}Cr_{34}Ni_{14}Al_{14}Co_4$ high-entropy alloy with good compressive mechanical properties, Mater. Sci. Eng. 716 (2018) 235–239, https://doi.org/10.1016/j.msea.2018.01.034.

[37] T. Xiong, W.F. Yang, S.J. Zheng, Z.R. Liu, Y.P. Lu, R.F. Zhang, Y.T. Zhou, X.H. Shao, B. Zhang, J. Wang, F.X. Yin, P.K. Liaw, X.L. Ma, Faceted Kurdjumov-Sachs interface-induced slip continuity in the eutectic high-entropy alloy, AlCoCrFeNi2.1, J. Mater. Sci. Technol. 65 (2021) 216–227, https://doi.org/10.1016/j.jmst.2020.04.073.

[38] Q.F. Wu, Z.J. Wang, T. Zheng, D. Chen, Z.S. Yang, J.J. Li, J.J. Kai, J.C. Wang, A casting eutectic high entropy alloy with superior strength-ductility combination, Mater. Lett. 253 (2019) 268–271, https://doi.org/10.1016/j.matlet.2019.06.067.

[39] H. Jiang, L. Jiang, D.X. Qiao, Y.P. Lu, T.M. Wang, Z.Q. Cao, T.J. Li, Effect of niobium on microstructure and properties of the CoCrFeNbxNi high entropy alloys, J. Mater. Sci. Technol. 33 (2017) 712–717, https://doi.org/10.1016/j.jmst.2016.09.016.

[40] Y. Liao, I. Baker, Microstructure and room-temperature mechanical properties of $Fe_{30}Ni_{20}Mn_{35}Al_{15}$, Mater. Char. 59 (2008) 1546–1549, https://doi.org/10.1016/j.matchar.2008.01.017.

[41] F. He, Z. Wang, P. Cheng, Q. Wang, J. Li, Y. Dang, J. Wang, C.T. Liu, Designing eutectic high entropy alloys of $CoCrFeNiNb_x$, J. Alloys Compd. 656 (2016) 284–289, https://doi.org/10.1016/j.jallcom.2015.09.153.

[42] H. Jiang, H. Zhang, T. Huang, Y. Lu, T. Wang, T. Li, Microstructures and mechanical properties of $Co_2Mo_xNi_2VW_x$ eutectic high entropy alloys, Mater. Des. 109 (2016) 539–546, https://doi.org/10.1016/j.matdes.2016.07.113.

[43] L. Jiang, Z.Q. Cao, J.C. Jie, J.J. Zhang, Y.P. Lu, T.M. Wang, T.J. Li, Effect of Mo and Ni elements on microstructure evolution and mechanical properties of the $CoFeNi_xVMo_y$ high entropy alloys, J. Alloys Compd. 649 (2015) 585–590, https://doi.org/10.1016/j.jallcom.2015.07.185.

[44] L. Jiang, Y.P. Lu, Y. Dong, T. Wang, Z. Cao, T. Li, Effects of Nb addition on structural evolution and properties of the $CoFeNi_2V_{0.5}$ high-entropy alloy, Appl. Phys. A 119 (2015) 291–297, https://doi.org/10.1007/s00339-014-8964-4.

[45] W. Huo, H. Zhou, F. Fang, X. Zhou, Z. Xie, J. Jiang, Microstructure and properties of novel $CoCrFeNiTa_x$ eutectic high-entropy alloys, J. Alloys Compd. 735 (2018) 897–904, https://doi.org/10.1016/j.jallcom.2017.11.075.

[46] Y. Lu, M.D. Zhang, L.J. Zhang, P.F. Yu, R. Li, X.S. Liu, Y.F. Zhang, G. Li, Cobalt-element-free eutectic medium-entropy alloys with superior mechanical performance and processability, Mater. Sci. Eng. 801 (2021) 140421, https://doi.org/10.1016/j.msea.2020.140421.

[47] W. Jiao, H. Jiang, D. Qiao, J. He, H. Zhao, Y. Lu, T. Li, Effects of Mo on microstructure and mechanical properties of Fe_2Ni_2CrMox eutectic high entropy alloys, Mater. Chem. Phys. 260 (2021) 124175, https://doi.org/10.1016/j.matchemphys.2020.124175.

[48] H. Gasan, A. Ozcan, New eutectic high-entropy alloys based on Co-Cr-Fe-Mo-Ni-Al: design, characterization and mechanical properties, Met. Mater. Int. 26 (2020) 1152–1167, https://doi.org/10.1007/s12540-019-00515-9.

[49] S. Muskeri, V. Hasannaeimi, R. Salloom, M. Sadeghilaridjani, S. Mukherjee, Small scale mechanical behavior of a eutectic high entropy alloy, Sci. Rep. 10 (2020) 2669, https://doi.org/10.1038/s41598-020-59513-2.

[50] X. Chen, J.Q. Qi, Y.W. Sui, Y.Z. He, F.X. Wei, Q.K. Meng, Z. Sun, Effects of aluminum on microstructure and compressive properties of Al-Cr-Fe-Ni eutectic multi-component alloys, Mater. Sci. Eng. 681 (2017) 25–31, https://doi.org/10.1016/j.msea.2016.11.019.

[51] T. Xie, Z. Xiong, Z. Xu, Z. Liu, X. Cheng, Another eutectic point of Co-Cr-Fe-Ni-M (Hf, Ta, Nb) high-entropy system determined using a simple mixture method correlated with mixing enthalpy, Mater. Sci. Eng. 802 (2021) 140634, https://doi.org/10.1016/j.msea.2020.140634.

[52] W. Huo, H. Zhou, F. Fang, X. Zhou, Z. Xie, J. Jiang, Microstructure and properties of novel $CoCrFeNiTa_x$ eutectic high-entropy alloys, J. Alloys Compd. 735 (2018) 897–904, https://doi.org/10.1016/j.jallcom.2017.11.075.

[53] L. Jiang, Y. Lu, W. Wu, Z. Cao, T. Li, Microstructure and mechanical properties of a CoFeNi2V0.5Nb0.75 eutectic high entropy alloy in as-cast and heat-treated conditions, J. Mater. Sci. Technol. 32 (2016) 245–250, https://doi.org/10.1016/j.jmst.2015.08.006.

[54] H. Ren, R.R. Chen, X.F. Gao, T. Liu, G. Qin, S.P. Wu, J.J. Guo, High-performance AlCoCrFeNi high entropy alloy with marine application perspective, J. Mater. Res. Technol. 25 (2023) 6751–6763, https://doi.org/10.1016/j.jmrt.2023.07.135.

[55] H.D. Wang, W. Zhang, P. Gao, Q.C. Xiang, Y.D. Qu, J.C. Cheng, Y.L. Ren, B. Yu, K. Q. Qiu, AlxCrFeNi medium entropy alloys with high damping capacity, J. Alloys Compd. 876 (2021) 159991, https://doi.org/10.1016/j.jallcom.2021.159991.

[56] Q. Wang, Y. Ma, B.B. Jiang, X.N. Li, Y. Shi, C. Dong, P.K. Liaw, A cuboidal B2 nanoprecipitation-enhanced body-centered-cubic alloy $Al_{0.7}CoCrFe_2Ni$ with prominent tensile properties, Scripta Mater. 120 (2016) 85–89, https://doi.org/10.1016/j.scriptamat.2016.04.014.

[57] J. Chen, B. Young, Stress-strain curves for stainless steel at elevated temperatures, Eng. Struct. 28 (2006) 229–239, https://doi.org/10.1016/J.ENGSTRUCT.2005.07.005.

[58] C. Leyens, M. Peters, Titanium and Titanium Alloys e Fundamentals and Applications, Wiley-VCH Verlag GmbH & Co. KGaA, Weinheim, 2003, https://doi.org/10.1002/3527602119.

[59] Y. Zhou, X. Jin, L. Zhang, X.Y. Du, B.S. Lia, A hierarchical nanostructured $Fe_{34}Cr_{34}Ni_{14}Al_{14}Co_4$ high-entropy alloy with good compressive mechanical properties, Mater. Sci. Eng. 716 (2018) 235–239, https://doi.org/10.1016/j.msea.2018.01.034.

[60] S. Wee, J. Do, K. Kim, C. Lee, C. Seok, B. Choi, Y. Choi, W. Kim, Review on mechanical thermal properties of superalloys and thermal barrier coating used in gas Turbines, Appl. Sci. 10 (2020) 5476.

[61] B. Chen, X.M. Li, Y.Y. Niu, R. Yang, W.J. Chen, B. Yusupu, L.M. Jia, A dual-phase CrFeNbTiMo refractory high entropy alloy with excellent hardness and strength, Mater. Lett. 337 (2023) 133958, https://doi.org/10.1016/j.matlet.2023.133958.

[62] K.B. Zhang, Z.Y. Fu, J.Y. Zhang, W.M. Wang, H. Wang, Y.C. Wang, Q.J. Zhang, J. Shi, Microstructure and mechanical properties of CoCrFeNiTiAlx high-entropy alloys, Mater. Sci. Eng. 508 (2009) 214–219, https://doi.org/10.1016/j.msea.2008.12.053.

[63] L.H. Wen, H.C. Kou, J.S. Li, H. Chang, X.Y. Xue, L. Zhou, Effect of aging temperature on microstructure and properties of AlCoCrCuFeNi high-entropy alloy, Intermetallics 17 (2009) 266–269.

[64] Y. Zhang, Y.J. Zhou, J.P. Lin, G.L. Chen, P.K. Liaw, Solid-solution phase formation rules for multi-component alloys, Adv. Eng. Mater. 10 (2008) 534–538, https://doi.org/10.1002/adem.200700240.

[65] M.X. Ren, B.S. Li, H.Z. Fu, Formation condition of solid solution type high-entropy alloy, Trans. Nonferrous Metals Soc. China 23 (2013) 991–995, https://doi.org/10.1016/S1003-6326(13)62557-1.

[66] S. Guo, C. Ng, J. Lu, C.T. Liu, Effect of valence electron concentration on stability of fcc or bcc phase in high entropy alloys, J. Appl. Phys. 109 (2011) 103505, https://doi.org/10.1063/1.3587228.

[67] X. Yang, Y. Zhang, Prediction of high-entropy stabilized solid-solution in multicomponent alloys, Mater. Chem. Phys. 132 (2012) 233–238, https://doi.org/10.1016/j.matchemphys.2011.11.021.
[68] G. Sheng, C. Ng, L. Jian, C.T. Liu, Effect of valence electron concentration on stability of fcc or bcc phase in high entropy alloys, J. Appl. Phys. 109 (2011) 213, https://doi.org/10.1063/1.3587228.
[69] J.W. Yeh, Recent progress in high-entropy alloys, Ann. Chim. Sci. Mat. 31 (2006) 633–648.
[70] Y. Zhang, Y.J. Zhou, Solid solution formation criteria for high entropy alloys, Mater. Sci. Forum 561 (2007) 1337–1339. https://doi.org/10.4028/www.scientific.net/MSF.561-565.1337.
[71] Y.F. Ye, Q. Wang, J. Lu, C.T. Liu, Y. Yang, High-entropy alloy: challenges and Prospects, Mater. Today 19 (2016) 349–362, https://doi.org/10.1016/j.mattod.2015.11.026.
[72] G.Y. Ke, S.K. Chen, T. Hsu, J.W. Yeh, FCC and BCC equivalents in as-cast solid solutions of AlxCoyCrzCu0.5FevNiw high-entropy alloys, Ann. Chim-Sci. Mat. 31 (2006) 669–684, https://doi.org/10.3166/acsm.31.669-684.
[73] C.C. Tung, J.W. Yeh, T.T. Shun, S.K. Chen, Y.S. Huang, H.C. Chen, On the elemental effect of AlCoCrCuFeNi high-entropy alloy system, Mater. Lett. 61 (2007) 1–5, https://doi.org/10.1016/j.matlet.2006.03.140.
[74] O.N. Senkov, G.B. Wilks, D.B. Miracle, C.P. Chuang, P.K. Liaw, Refractory high-entropy alloys, Intermetallics 18 (2010) 1758–1765, https://doi.org/10.1016/j.intermet.2010.05.014.
[75] C. Li, J.C. Li, M. Zhao, L. Zhang, Q. Jiang, Microstructure and properties of $AlTiNiMnB_x$ high entropy alloys, Mater. Sci. Technol. 24 (2008) 376–378, https://doi.org/10.1179/174328408X275964.
[76] B. Cantor, I.T.H. Chang, P. Knight, A.J.B. Vincent, Microstructural development in equiatomic multicomponent alloys, Mater. Sci. Eng. 375–377 (2004) 213–218, https://doi.org/10.1016/j.msea.2003.10.257.
[77] M. Yang, D. Yan, F. Yuan, P. Jiang, E. Ma, X. Wu, Dynamically reinforced heterogeneous grain structure prolongs ductility in a medium-entropy alloy with gigapascal yield strength, Proc. Natl. Acad. Sci. USA 115 (2018) 7224–7229, https://doi.org/10.1073/pnas.1807817115.
[78] K. Lu, Making strong nanomaterials ductile with gradients, Science 345 (2014) 1455–1456, https://doi.org/10.1126/science.1255940.
[79] E. Ma, T. Zhu, Towards strength-ductility synergy through the design of heterogeneous nanostructures in metals, Mater. Today 20 (2017) 323–331, https://doi.org/10.1016/j.mattod.2017.02.003.
[80] M.X. Yang, F.P. Yuan, Q.G. Xie, Y.D. Wang, E. Ma, X.L. Wu, Strain hardening in Fe-16Mn-10Al-0.86C-5Ni high specific strength steel, Acta Mater. 109 (2016) 213–222, https://doi.org/10.1016/j.actamat.2016.02.044.
[81] X. Wu, Y. Zhu, Heterogeneous materials: a new class of materials with unprecedented mechanical properties, Mater. Res. Lett. 5 (2017) 527–532, https://doi.org/10.1080/21663831.2017.1343208.
[82] Y.P. Lu, X.Z. Gao, L. jiang, Z.N. Chen, T.M. Wang, J.C. Jie, H.J. Kang, Y.B. Zhang, S. Guo, H.H. Ruan, Y.H. Zhao, Z.Q. Cao, T.J. Li, Directly cast bulk eutectic and near-eutectic high entropy alloys with balanced strength and ductility in a wide temperature range, Acta Mater. 124 (2017) 143–150, https://doi.org/10.1016/j.actamat.2016.11.016.
[83] I. Baker, A review of the mechanical properties of B2 compounds, Mater. Sci. Eng., A 192–193 (1995) 1–13, https://doi.org/10.1016/0921-5093(94)03200-9.
[84] D.G. Shaysultanov, G.A. Salishchev, YuV. Ivanisenko, S.V. Zherebtsov, M. A. Tikhonovsky, N.D. Stepanov, Novel $Fe_{36}Mn_{21}Cr_{18}Ni_{15}Al_{10}$ high entropy alloy with bcc/B2 dual-phase structure, J. Alloys Compd. 705 (2017) 756–763, https://doi.org/10.1016/j.jallcom.2017.02.211.
[85] L.X. Liu, Z.J. Wang, Q.F. Wu, Y.H. Jia, Q. Xu F. He, J.J. Li, J.C. Wang, A hypoeutectic high-entropy alloy with hierarchical microstructure for high-temperature application, Scripta Mater. 232 (2023) 115502, https://doi.org/10.1016/j.scriptamat.2023.115502.
[86] R. Feng, Y. Rao, C.H. Liu, X. Xie, D.J. Yu, Y. Chen, M. Ghazisaeidi, T. Ungar, H. M. Wang, K. An, P.K. Liaw, Enhancing fatigue life by ductile-transformable multicomponent B2 precipitates in a high-entropy alloy, Nat. Commun. 12 (2021) 3588, https://doi.org/10.1038/s41467-021-23689-6.
[87] T. Bhattacharjee, I.S. Wani, S. Sheikh, I.T. Clark, T. Okawa, S. Guo, P. P. Bhattacharjee, N. Tsuji, Simultaneous strength-ductility enhancement of a Nano-lamellar AlCoCrFeNi2.1 eutectic high entropy alloy by Cryo-rolling and annealing, Sci. Rep. 8 (2018) 3276, https://doi.org/10.1038/s41598-018-21385-y.
[88] I. Basu, J.T.M. DeHosson, Strengthening mechanisms in high entropy alloys: fundamental issues, Scripta Mater. 187 (2020) 148–156, https://doi.org/10.1016/j.scriptamat.2020.06.019.
[89] D. Caillard, Dynamic strain ageing in iron alloys: the shielding effect of carbon, Acta Mater. 112 (2016) 273–284, https://doi.org/10.1016/j.actamat.2016.04.018.
[90] M.A. Soare, W.A. Curtin, Solute strengthening of both mobile and forest dislocations: the origin of dynamic strain aging in fcc metals, Acta Mater. 56 (2008) 4046–4061, https://doi.org/10.1016/j.actamat.2008.04.027.
[91] B.X. Cao, D.X. Wei, X.F. Zhang, H.J. Kong, Y.L. Zhao, J.X. Hou, J.H. Luan, Z.B. Jiao, Y. Liu, T. Yang, C.T. Liu, Intermediate temperature embrittlement in a precipitation-hardened high-entropy alloy: the role of heterogeneous strain distribution and environmentally assisted intergranular damage, Mater. Today. Phys. 24 (2022) 100653, https://doi.org/10.1016/j.mtphys.2022.100653.
[92] X.J. Guan, F. Shi, H.M. Ji, X.W. Li, A possibility to synchronously improve the high-temperature strength and ductility in face-centered cubic metals through grain boundary engineering, Scripta Mater. 187 (2020) 216–220, https://doi.org/10.1016/j.scriptamat.2020.06.026.
[93] D. Lin, Q. Chen, X. Xi, R. Ma, Z. Shi, X. Song, H. Xia, H. Bian, C. Tan, Y. Lu, R. Li, Laser powder bed fusion to fabricate high-entropy alloy$FeCoCrNiMo_{0.5}$ with excellent high-temperature strength and ductility, Mater. Sci. Eng. (2024) 146413, https://doi.org/10.1016/j.msea.2024.146413.
[94] Z. Xu, Z. Li, Y. Tong, W. Zhang, Z. Wu, Microstructural and mechanical behavior of a CoCrFeNiCu4 non-equiatomic high entropy alloy, J. Mater. Sci. Technol. 60 (2021) 35–43, https://doi.org/10.1016/j.jmst.2020.03.078.